All-particle primary energy spectrum in the 3-200 PeV energy range

A.P. Garyaka [a], R.M. Martirosov [a], S.V. Ter-Antonyan [b,*],
A.D. Erlykin [c], N.M. Nikolskaya [c], Y.A. Gallant [d], L.W. Jones [e]
and J. Procureur [f]

[a] *Yerevan Physics Institute, 2 Alikhanyan Br. Str., 375036 Yerevan, Armenia*

[b] *Department of Physics, Southern University, Baton Rouge, USA*

[c] *P.N.Lebedev Physical Institute, Moscow, Russia*

[d] *LPTA, Université Montpellier II, CNRS/IN2P3, Montpellier, France*

[e] *University of Michigan, Department of Physics, USA*

[f] *Centre d'Etudes Nucléaires de Bordeaux-Gradignan, Gradignan, France*

Abstract

We present all-particle primary cosmic-ray energy spectrum in the $3 \cdot 10^6 - 2 \cdot 10^8$ GeV energy range obtained by a multi-parametric event-by-event evaluation of the primary energy. The results are obtained on the basis of an expanded EAS data set detected at mountain level (700 g/cm^2) by the GAMMA experiment. The energy evaluation method has been developed using the EAS simulation with the SIBYLL interaction model taking into account the response of GAMMA detectors and reconstruction uncertainties of EAS parameters. Nearly unbiased ($< 5\%$) energy estimations regardless of a primary nuclear mass with an accuracy of about $15-10\%$ in the $3 \cdot 10^6 - 2 \cdot 10^8$ GeV energy range respectively are attained.

An irregularity ('bump') in the spectrum is observed at primary energies of $\sim 7.4 \cdot 10^7$ GeV. This bump exceeds a smooth power-law fit to the data by about 4 standard deviations. Not rejecting stochastic nature of the bump completely, we examined the systematic uncertainties of our methods and conclude that they cannot be responsible for the observed feature.

Key words: Cosmic rays, energy spectra, composition, extensive air showers
  PACS: 96.40.Pq, 96.40.De, 96.40.-z, 98.70.Sa

---

* Corresponding author:
  Email address: `samvel_terantonyan@subr.edu` (S.V. Ter-Antonyan).

arXiv:0808.1421v1 [astro-ph] 10 Aug 2008

1 Introduction

Study of the fine structure in the primary energy spectrum is one of the most important tasks in the very high energy cosmic ray experiments [1]. Commonly accepted values of the all-particle energy spectrum indexes of -2.7 and -3.1 before and after the knee are an average and may not reflect the real behavior of the spectrum particularly after the knee. It is necessary to pay special attention to the energy region of $(1-10) \cdot 10^7$ GeV, where experimental results have been very limited up to now. Irregularities of the energy spectrum in this region were observed a long time ago. They can be seen from energy spectrum obtained more than 20 years ago with AKENO experiment [2] as well as in later works of the GAMMA [3] and TUNKA [4] experiments. At the same time the large statistical errors did not allow to discuss the reasons of these irregularities.

On the other hand results of many experiments on the study of EAS charge particle spectra, the behavior of the age parameter and muon component characteristics point out that the primary mass composition at energies above the knee becomes significantly heavier. Based on these indications, additional investigations of the fine structure of the primary energy spectrum at $(1-10) \cdot 10^7$ GeV have an obvious interest.

There are two ways to obtain the primary energy spectra using detected extensive air showers (EAS). The first way is a statistical method, which unfolds the primary energy spectra from the corresponding integral equation set based on a detected EAS data set and the model of the EAS development in the atmosphere [5,6,7,8,9]. The second method is based on an event-by-event evaluation [2,10,11,12,13] of the primary energy of the detected EAS with parameters $\mathbf{q} \equiv q(N_e, N_\mu, N_h, s, \theta)$ using parametric $E = f(\mathbf{q})$ [2,10,11,13] or non-parametric [12] energy estimator previously determined on the basis of shower simulations in the framework of a given model of EAS development.

Here, applying a new event-by-event parametric energy evaluation $E = f(\mathbf{q})$, the all-particle energy spectrum in the knee region is obtained on the basis of the data set obtained with the GAMMA EAS array [7,8,9,11] and a simulated EAS database obtained using the SIBYLL [14] interaction model. Preliminary results have been presented in [10,11].

2 GAMMA experiment

The GAMMA installation [7,8,9,11] is a ground based array of 33 surface detection stations and 150 underground muon detectors, located on the south side of Mount Aragats in Armenia. The elevation of the GAMMA facility is 3200 m above sea level, which corresponds to 700 g/cm^2 of atmospheric depth. A diagrammatic layout of the array is shown in Fig. 1.
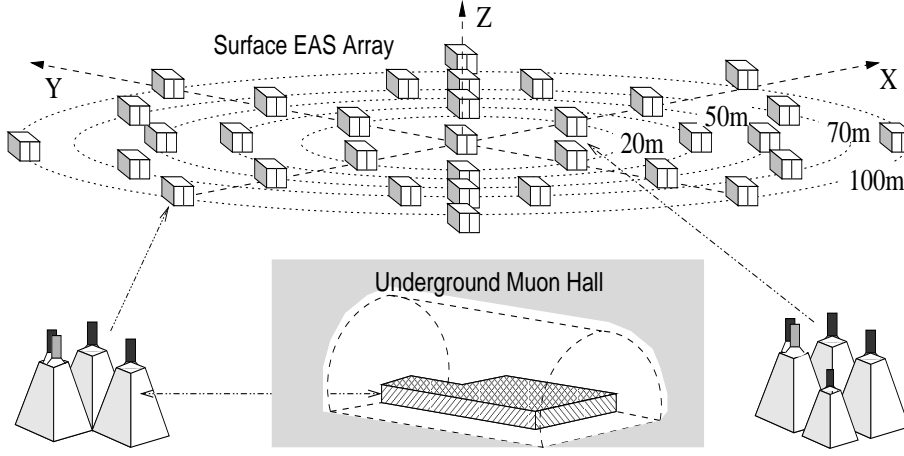
Fig. 1. Diagrammatic layout of the GAMMA facility.

The surface stations of the EAS array are arranged in 5 concentric circles of $\sim$20, 28, 50, 70 and 100 m radii, and each station contains 3 plastic scintillation detectors with the dimensions of $1 \times 1 \times 0.05$ m^3. Each of the central 9 stations contains an additional (the 4th) small scintillator with dimensions of $0.3 \times 0.3 \times 0.05$ m^3 (Fig. 1) for high particle density ($\gg 10^2$ particles/m^2) measurements.

A photomultiplier tube is placed on the top of the aluminum casing covering each scintillator. One of three detectors of each station is viewed by two photomultipliers, one of which is designed for fast timing measurements.

150 underground muon detectors ('muon carpet') are compactly arranged in the underground hall under 2.3 kg/cm^2 of concrete and rock. The scintillator dimensions, casings and photomultipliers are the same as in the EAS surface detectors.

The shower size thresholds of the 100% shower detection efficiency are equal to $N_{ch} = 3 \cdot 10^5$ and $N_{ch} = 5 \cdot 10^5$ at the EAS core location within $R < 25$ m and $R < 50$ m respectively [7,8,11].

The time delay is estimated by the pair-delay method [15] to give the time resolution of about $4 - 5$ ns. The EAS detection efficiency (P_d) and corresponding shower parameter reconstruction errors are equal to: $P_d = 100\%$, $\Delta\theta \simeq 1.5^0$, $\Delta N_{ch}/N_{ch} \simeq 0.05 - 0.15$, $\Delta s \simeq 0.05$, Δx and $\Delta y \simeq 0.7 - 1$ m. The reconstruction errors of the truncated muon shower sizes for $R_\mu < 50$ m from the shower core are equal to $\Delta N_\mu/N_\mu \simeq 0.2 - 0.35$ at $N_\mu \simeq 10^5 - 10^3$ respectively [8,9,11].

3 Event-by-event energy estimation

3.1 Key assumptions

Suppose that $E_1 = f(\mathbf{q})$ is an estimator of energy E_0 of unknown primary nuclei which induced showers with the detected parameter $\mathbf{q} \equiv q(N_{ch}, N_\mu, s, \theta)$. Then the expected all-particle energy spectrum $F(E_1)$ is defined by

$$F(E_1) = \int \Im(E_0) W(E_0, E_1) \, \mathrm{d}E_0 \,, \tag{1}$$

where $\Im(E_0)$ are the energy spectrum of primary nuclei and $W(E_0, E_1)$ are the corresponding (E_0, E_1) transformation probability density function.

If $\Im(E_0) \propto E_0^{-\gamma}$ and $W(E_0, E_1)$ are the log-normal distributions with $\delta = E_1/E_0$ and σ parameters, the expression (1) has the analytic solution for the expected spectrum of the energy estimator [16]:

$$F(E_1) = \Im(E_0) \delta^{\gamma-1} \exp\left(\frac{((\gamma-1)\sigma)^2}{2}\right). \tag{2}$$

It is seen that evaluation of energy spectrum $\Im(E_0)$ from (2) is possible to perform only at *a priori* known γ, δ and σ parameters and spectral slope (γ) of detected energy spectra $F(E_1)$ coincides with spectral slope of primary energy spectra $\Im(E_0)$. The values of δ and σ may depend on the primary energy (E_0) and mass of primary nuclei (A) from which the all-particle energy spectrum $\Im(E_0) = \sum_A \Im_A(E_0)$ is consisted of. In this case, the expression (1) is unfolded numerically and the slope of detected energy spectrum can differ from primary energy spectrum.

For example, the dependence $\sigma(E_0) = a \ln(E_0/E_{0,\min}) + b$ at $|a| < 0.1$ leads to the numerical solutions which can be approximated by the expression (2) replacing σ with $\sigma(E_0) - a\sqrt{\gamma}$. The corresponding approximation errors is about $2 - 5\%$ in the energy range of $E_{\min} - 500 E_{\min}$ and $\gamma \simeq 2.3 - 3.2$.

However, the evaluation of energy spectra can be simplified provided

$$\gamma(E_0) \simeq \gamma \pm \Delta\gamma, \tag{3}$$

$$\delta(E_0) \simeq \delta_A(E_1) \simeq \delta \equiv 1 \pm \Delta\delta(E_1), \tag{4}$$

$$\sigma(E_0) \simeq \sigma \pm \Delta\sigma \tag{5}$$

are satisfied for given energy range of E_1. Then, the all-particle energy spectrum can be evaluated from

$$\Im(E_0) = F(E_1) \exp\left(-\frac{((\gamma-1)\sigma)^2}{2}\right). \tag{6}$$

The corresponding error of evaluation (6) with approaches (3-5) is determined by a sum of the statistical errors $\Delta F(E_1)$ and systematic errors η due to approaches being used:

$$\left(\frac{\Delta\Im}{\Im}\right)^2 \simeq \left(\frac{\Delta F}{F}\right)^2 + \eta^2,$$

where the systematic relative errors η is

$$\eta^2 \simeq (\Delta\delta(\gamma-1))^2 + [(\sigma(\gamma-1))^2(\frac{\Delta\sigma}{\sigma} + \frac{\Delta\gamma}{\gamma-1})]^2. \tag{7}$$

The values of γ, δ and σ parameters from expressions (3-7) and corresponding uncertainties $\Delta\gamma$, $\Delta\delta$ and $\Delta\sigma$ essential for the reconstruction of primary energy spectrum using the GAMMA facility EAS data and approach (6) are considered in Sections 3.2-3.4 below.

3.2 Uncertainty of spectral slope

The results of different experiments [9,17,18,19] and theoretical predictions [20,21,22] indicate that the elemental energy spectra can be presented in the power law form

$$\Im_A(E) \propto \left(\frac{E}{E_k}\right)^{-\gamma}, \tag{8}$$

where $\gamma = \gamma_1 \simeq 2.7^{+0.05}_{-0.1}$ at $E < E_k(A)$ and $\gamma = \gamma_2 \simeq 3.15^{+0.1}_{-0.05}$ at $E > E_k(A)$. It is also accepted that the mass spectra of primary nuclei can be divided into separate nuclear groups and below, as in [9], just 4 nuclear species (H, He, O-like and Fe-like) are considered. Dependence of the knee energy E_k on the primary nuclei type assumed to be either rigidity dependent, $E_k = ZE_{Z=1}$ [9,20,21,22] or A-dependent [9,23], $E_k = AE_{A=1}$, where Z and A are the charge and mass of primary nuclei correspondingly.

As a result, the all-particle energy spectrum $\sum_A \Im_A(E)$ slowly changes its slope and can be roughly approximated by a power law spectrum with power index $\gamma \simeq 2.7$ at $E < 3 \cdot 10^6$ GeV, $\gamma \simeq 2.9$ at $3 \cdot 10^6 < E < 10^7$ GeV and $\gamma \simeq 3.1$ at $E > 10^7$ GeV. This presentation of the all-particle spectrum agrees

with world data [23] in the $\Delta\gamma \simeq 0.1$ range of uncertainty and energy interval $10^6 < E < 2 \cdot 10^8$ GeV.

The values of $\Delta\delta_A(E)$ and $\sigma_A(E_0)$ parameters are presented in Section 3.4 and depend on efficiency of energy estimator $E_1 = f(N_{ch}, N_\mu, s, \theta)$.

Notice that it follows from the expression (7) that for $\sigma \simeq 0.1 - 0.15$ and $\Delta\sigma = 0.03$ the contribution of $\Delta\gamma$ in the systematic errors (7) is negligible and the difference of all-particle spectra evaluated by expression (6) for $\gamma = 2.7$ and $\gamma = 3.1$ is less than 2% at $\sigma \simeq 0.15$.

3.3 The simulated EAS database

To obtain the parametric representation for unbiased ($\delta \simeq 1$) energy estimator E_1 of the primary energy E_0 we simulated showers database using the CORSIKA(NKG) EAS simulation code [24] with the SIBYLL [14] interaction model for H, He, O and Fe primary nuclei.

Preliminary, the showers simulated with NKG mode of CORSIKA code for each of the primary nuclei were compared with the corresponding simulations using EGS mode of CORSIKA [24] taking into account the detector response, contribution of EAS γ-quanta and shower parameter reconstruction uncertainties. Simulated statistics were equal to 200 events for each of primary nuclei with log-uniform primary energy distribution in the range of $2 \cdot 10^6 - 10^8$ GeV. Using the threshold energy of shower electrons (positrons) for NKG mode at observation level as a free parameter (the same as it was performed in [9]), the biases $\delta(N_{ch}, A) = (N_{ch}(NKG)/N_{ch}(EGS)) - 1)$ and $\delta_s(A) = s(NKG) - s(EGS)$ were minimized for all simulated primary nuclei (H, He, O, Fe).

Applied method of calibration of the NKG mode of CORSIKA for the GAMMA EAS array differed from [9] only by the expanded range of selected shower core coordinates ($R < 50m$) and zenith angles $\theta < 45^0$. The obtained biases of shower size $\delta(N_{ch})$ and age parameter s in the range of statistical errors ($< 5\%$) agreed with data [9]. The values of $\delta(N_{ch})$ were used further for correction of the shower size obtained by NKG simulation mode.

The simulated primary energies (E_0) for shower database were distributed according to a power law spectrum $I(E_0) \propto E_0^{-1.5}$ with $\mathcal{N} = 2 \cdot 10^4$ total number of detected ($N_{ch} > 5 \cdot 10^5$, $R < 50m$) and reconstructed showers for each primary nucleus. The energy thresholds of primary nuclei were set as $E_{0,\min}(A) \equiv 10^6$ GeV and $E_{\max} = 5 \cdot 10^8$ GeV. The simulated showers had core coordinates distributed uniformly within the radius of $R < 75$ m and zenith angles $\theta < 45^0$.

The reconstruction errors $\sigma(\ln N_{ch})$ of shower size N_{ch} are presented in Fig. 2 for different primary nuclei and different zenith angles. The right and left ends of diagonals of the rectangular in Fig. 2 show the average primary
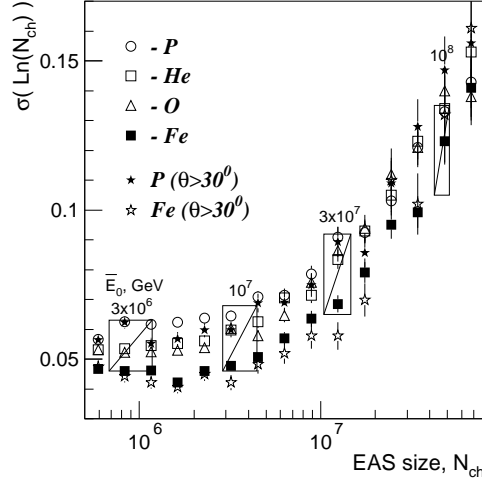
6

Fig. 2. Shower size reconstruction errors for different primary nuclei (p, He, O, Fe) and zenith angles $(\theta < 45^0$ and $30^0 < \theta < 45^0)$. The right and left ends of diagonals of the rectangular show the average primary energies $(\overline{E_0})$ and corresponding shower sizes computed for the primary proton and Iron nuclei respectively.

energies (in units of GeV) responsible for corresponding shower sizes for the primary proton and Iron nuclei respectively.

All EAS muons with energies of $E_\mu > 4$ GeV at GAMMA observation level have passed through the 2.3 kg/cm^2 of rock to the muon scintillation carpet (the underground muon hall, Fig. 1). The muon ionization losses and electron (positron) accompaniment due to muon electromagnetic and photonuclear interactions in the rock are taken into account using the approximation for equilibrium accompanying charged particles obtained from preliminary simulations with the FLUKA code [26] in the $0.005 - 20$ TeV muon energy range. The resulting charged particle accompaniment per EAS muon in the underground hall is equal to 0.06 ± 0.01 ($100\%e$) and 11.0 ± 1.5 ($98.5\%e, 1.4\%h, 0.04\%\mu$) at muon energies 0.01 TeV and 10 TeV respectively.

Due to absence of saturation in the muon scintillation carpet, the reconstruction errors ($\Delta \ln N_\mu$) of truncated muon size N_μ are continuously decreasing with increasing muon truncated sizes in the range $10^3 < N_\mu < 10^5$. Corresponding magnitudes of reconstruction errors for primary protons and Iron nuclei were equal to $\Delta(\ln N_{\mu,p}) \simeq 0.35, 0.18, 0.15$ and $\Delta(\ln N_{\mu,Fe}) \simeq 0.38, 0.19, 0.10$ for EAS muon truncated sizes $N_\mu \simeq 10^3, 10^4, 10^5$ respectively.

Fluctuations of the shower size for given primary energies $E_{0,A} \equiv 10^6, 10^7, 10^8$ GeV and $\cos \theta < 0.95$ were equal to $\sigma_{A \equiv p}(N_{ch}, E_0) \simeq 0.20, 0.14, 0.10$ and $\sigma_{A \equiv Fe}(N_{ch}, E_0) \simeq 0.16, 0.13, 0.08$ respectively.

Corresponding fluctuations of muon truncated size were equal to $\sigma_{A \equiv p}(N_\mu, E_0) \simeq 0.25, 0.23, 0.2$ and $\sigma_{A \equiv Fe}(N_\mu, E_0) \simeq 0.13, 0.10, 0.08$. For zenith angles of primary nuclei $45^0 > \theta > 30^0$, the fluctuations are increased about $1.5 - 2$ times

7

Table 1

Correlation coefficients $\rho(\mathbf{q}, \ln E_0)$ and $\rho(\mathbf{q}, \ln A)$ between shower parameter $\mathbf{q} \equiv q(N_{ch}, N_\mu, s)$ and primary energy $(\ln E_0)$ and nuclei mass $\ln A$ for two zenith angular intervals.

$\mathbf{q}$	$\ln E_0, (\theta < 10^0)$	$\ln E_0, (\theta < 45^0)$	$\ln A, (\theta < 10^0)$	$\ln A, (\theta < 45^0)$
$\ln N_{ch}$	0.986 ± 0.001	0.954 ± 0.0004	0.013 ± 0.013	0.007 ± 0.004
$\ln N_\mu$	0.978 ± 0.001	0.969 ± 0.0003	0.139 ± 0.012	0.132 ± 0.004
s	-0.029 ± 0.013	-0.02 ± 0.004	0.018 ± 0.013	0.015 ± 0.004

due to the aging of detected showers.

The $4 \times 2 \cdot 10^4$ EAS simulated events with reconstructed N_{ch}, $N_\mu (R < 50\text{m})$, s and θ shower parameters for the E_0 and A parameters of primary nuclei made up the simulated EAS database.

3.4 Energy estimator

The event-by-event reconstruction of primary all-particle energy spectrum using the GAMMA facility is mainly based on high correlation of primary energy E_0 and shower size (N_{ch}). The shower age parameter (s) zenith angle (θ) and muon truncated shower size (N_μ) have to decrease the unavoidable biases of energy evaluations due to abundance of different primary nuclei. In Table 1 the correlation coefficients $\rho(\mathbf{q}, \ln E_0)$ and $\rho(\mathbf{q}, \ln A)$ between shower parameters N_{ch}, N_μ, s and primary energy (E_0) and mass of primary nuclei $(A \equiv 1, 4, 16, 56)$ are presented.

Parametric representation for the energy estimator $\ln E_1 \simeq f(\mathbf{a} | N_{ch}, N_\mu, s, \theta)$ we obtained by minimizing χ^2

$$\chi^2 = \sum_A \sum_{i=1}^{\mathcal{N}} \frac{(\ln E_{0,A,i} - \ln E_{1,i})^2}{\sigma^2} \qquad (9)$$

with respect to $\mathbf{a} \equiv a(a_1, a_2, \dots, a_p)$ for different empirical functions $f(\mathbf{a})$ with a different number (p) of unknown parameters. The values of A, E_0 and corresponding reconstructed shower parameters N_{ch}, N_μ, s and θ for estimation of E_1 were taken from simulated EAS database (Section 3.3).

The best energy estimations as a result of the minimization (9) were achieved for the 7-parametric $(p = 7)$ fit:

$$\ln E_1 = a_1 x + \frac{a_2 \sqrt{s}}{c} + a_3 + a_4 c + \frac{a_5}{(x - a_6 y)} + a_7 y e^s, \qquad (10)$$

8

Table 2

Approximation parameters $a_1, \ldots, a_7$ of primary energy evaluation (10) obtained from χ^2-minimization (9) for the SIBYLL interaction model, $\sigma = 0.14$ and $\chi^2_{\min}/n_{d.f.} \simeq 1$.

a_1	a_2	a_3	a_4	a_5	a_6	a_7
1.030	3.641	-5.743	2.113	6.444	1.200	-0.045
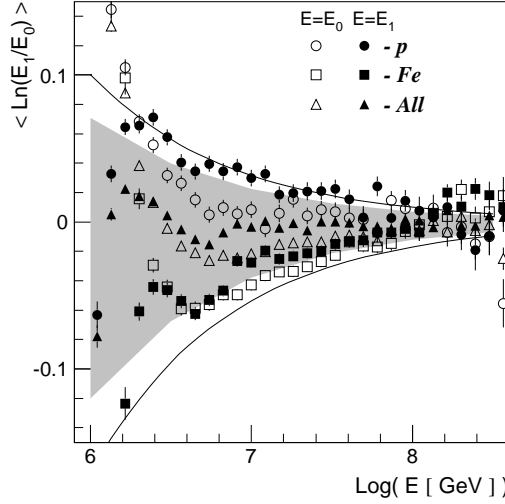
Fig. 3. Mean biases versus energy $E \equiv E_0$ and $E \equiv E_1$ for the primary proton (p) and iron (Fe) nucleus and the uniformly mixed p, He, O, Fe compositions (All).

where $x = \ln N_{ch}$, $y = \ln N_\mu(R < 50m)$, $c = \cos\theta$, s is the shower age and energy E_1 is in GeV. The values of $a_1, \ldots, a_7$ parameters are shown in Table 2 and were derived at $\sigma = 0.14$ and $\chi^2_{\min}/n_{d.f.} \simeq 1$, where the number of degrees of freedom $n_{d.f.} = 8 \cdot 10^4$. The expected errors $\Delta a_1, \ldots, \Delta a_7$ of corresponding parameters were negligibly small ($\leq 5\%$) due to very high values of $n_{d.f.}$.

The corresponding average biases versus energies ($E \equiv E_0$ and $E \equiv E_1$) for the primary proton (p), iron (Fe) nucleus and uniformly mixed p, He, O, Fe composition are presented in Fig. 3 (symbols). The boundary lines correspond to approximations $\Delta\delta \simeq b/\sqrt{E/10^6 GeV}$, where $b \simeq 0.10$ and $b \simeq -0.17$ for the upper and lower limits respectively. The shaded area corresponds to $b \simeq 0.09$ and $b \simeq -0.15$ and were used to estimate the errors according to (7) for the reconstruction of all-particle energy spectrum (Section 4).

The dependence of standard deviations $\sigma(E_0)$ of systematic errors of energy evaluations (10) on primary energy E_0 is presented in Fig. 4 for 4 primary nuclei and uniformly mixed composition with equal fractions of p, He, O and Fe nuclei. The results for the uniformly mixed composition with the shower core selection of $R < 25$ m [10] are presented in Fig. 4, as well. It is seen that the value of $\sigma = 0.14$ responsible for $\chi^2 \simeq 1$ (expression (9)) with uncertainty
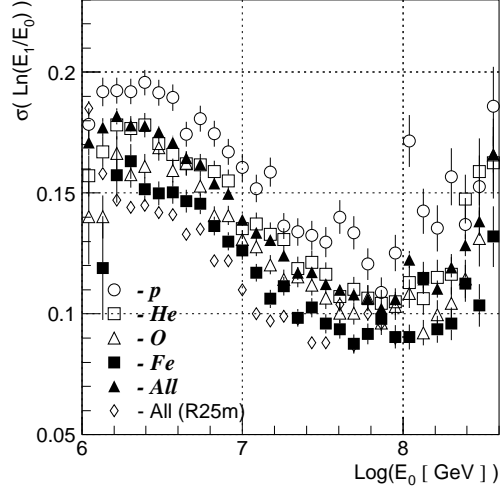
9

Fig. 4. Errors of the energy estimator (6) versus primary energy E_0 for 4 primary nuclei and uniformly mixed (*All*) composition. The empty rhombic symbols are taken from our previous data [10] computed for the mixed composition and shower core selection criteria $R < 25$m.
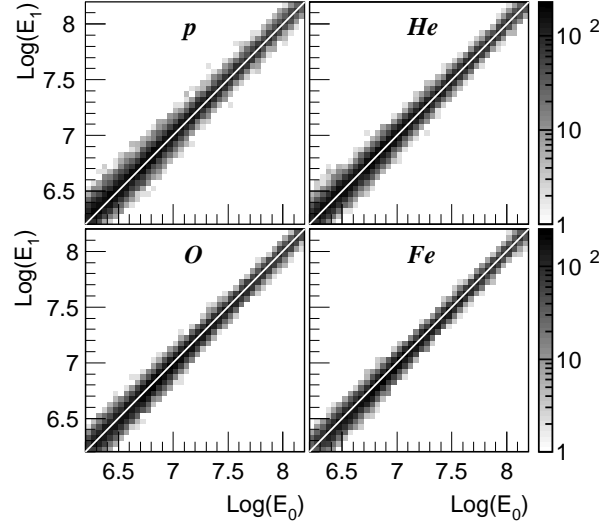

Fig. 5. $E_0 - E_1$ (in units of GeV) scatter plots for four (p, He, O, Fe) primary nuclei. The white lines show the corresponding $E_0 = E_1$ dependence.
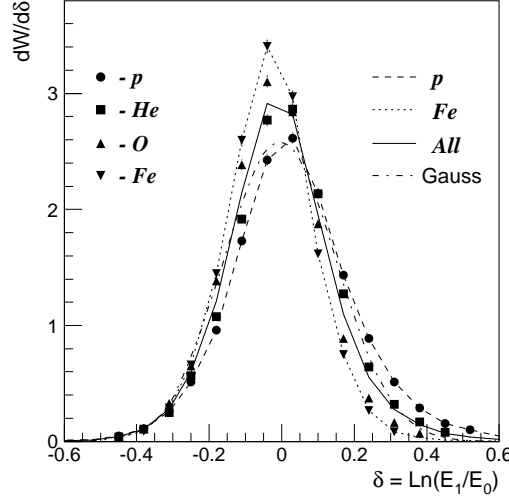
Fig. 6. Distribution functions of errors for different primary nuclei (symbols) and uniformly mixed composition (symbols and solid line).

$\Delta\sigma \simeq 0.03$ (expression (5)) encloses the $\sigma_A(E_0)$ data presented in Fig. 4.

Such high accuracies of the energy evaluation regardless of primary nuclei is a consequence of the high mountain location of the GAMMA facility (700 g/cm^2), where the correlation of primary energy with detected EAS size is about $0.95 - 0.99$ (Table 1).

The $E_0 - E_1$ scatter plot of simulated primary energy E_0 and estimated energy $E_1(N_{ch}, N_\mu, s, \theta)$ according to expression (10) and Table 2 are shown in Fig. 5. The corresponding distributions of energy errors or the kernel function $W_A(E_0, E_1|\delta_A, \sigma_A)$ of integral equation (1) for different primary nuclei and uniformly mixed composition are presented in Fig. 6 (symbols). The average values $\delta_A(E_0)$ and standard deviations $\sigma_A(E_0)$ of these distributions depending on energy of primary nucleus (A) are presented in Figs. 3,4. The dashed line is an example of log-normal distribution with δ and σ parameters corresponding to the uniformly mixed composition.

It is seen, that the errors can be described by the log-normal distributions and the key assumptions (3-5) are approximately valid.

The test of applied approaches (expressions (3-6), Section 3.2) for the reconstruction of all-particle primary energy spectrum was carried out by the direct folding of the power law energy spectrum $\Im(E_0) \equiv dF_0/dE_0$ (expression (8)) with the log-normal kernel function $W(E_0, E_1|\delta(E_0), \sigma(E_0))$ according to expression (1) for primary proton and Iron nucleus. The values of $\delta(E_0)$ and $\sigma(E_0)$ were derived from the log-parabolic interpolations of corresponding dependencies presented in Figs. 3,4. The event-by-event reconstructed energy spectrum dF_1/dE_1 (the left hand side of expression (1)) was obtained from expression (6) using approaches (3-5) with $\sigma = 0.14$ and $\Delta\sigma = 0.03$. The
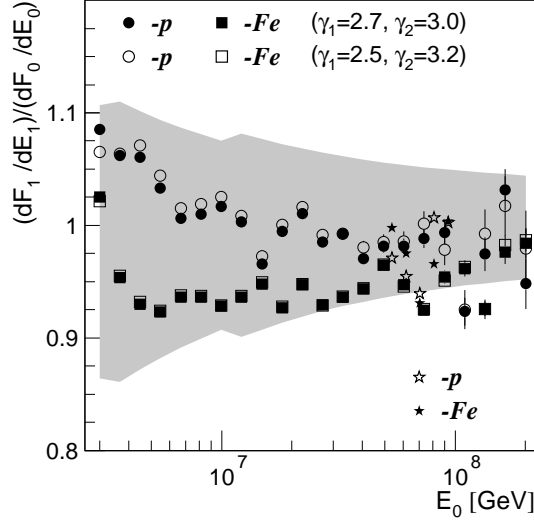
Fig. 7. Discrepancies of initial (dF_0/dE_0) and reconstructed (dF_1/dE_1) energy spectra (symbols) for the different primary nuclei and spectral indices of initial spectrum. The shaded area shows the expected errors according to expression (7). The star symbols are the spectral discrepancies for a pulsar component (Section 5).

boundary lines of shaded area in Fig. 3 were used as estimations of uncertainties $\Delta\delta(E_1)$ of condition (4). In Fig. 7 the values of $(dF_1/dE_1)/(dF_0/dE_0)$ are presented (symbols) for primary proton and Iron nuclei and different "unknown" spectral indices of primary energy spectra (8) with the rigidity dependent knee at $E_k = 3 \cdot 10^6$ GeV. The shades area is the expected errors computed according to expression (7). It is seen, that all spectral discrepancies are practically covered by the expected errors according to expression (7). The star symbols in Fig. 7 represent the discrepancies of singular spectra with knee at energy $7.4 \cdot 10^7$ GeV described in Section 5.

4 All-particle primary energy spectrum

The EAS data set analyzed in this paper has been obtained for $5.63 \cdot 10^7$ sec of live run time of the GAMMA facility, from 2004 to 2006. Showers to be analyzed were selected with the following criteria: $N_{ch} > 5 \cdot 10^5$, $R < 50$ m, $\theta < 45°$, $0.3 < s < 1.6$, $\chi^2(N_{ch})/m < 3$ and $\chi^2(N_\mu)/m < 3$ (where m is the number of scintillators with non-zero signal), yielding a total data set of $\sim 7 \cdot 10^5$ selected showers. The selected measurement range provided the 100% EAS detection efficiency and similar conditions for the reconstruction of showers produced by primary nuclei $H, He, \ldots, Fe$ with energies $3 \cdot 10^6 < E < (2-3) \cdot 10^8$
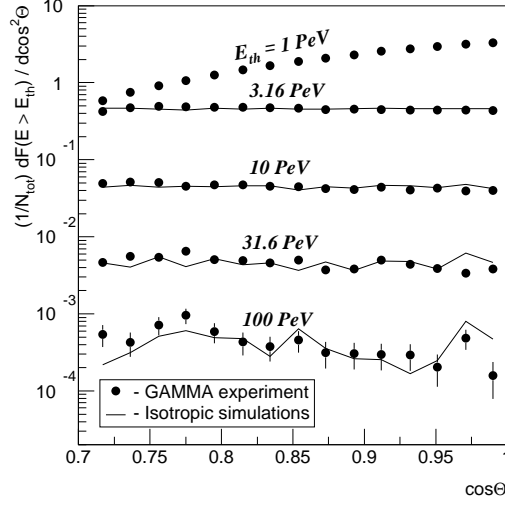
Fig. 8. Detected zenith angular distributions for different energy thresholds (symbols). The lines are corresponding simulated isotropic distributions with the same statistics.

GeV. The upper energy limit is determined from Fig. 4, where the saturation of surface scintillators in the shower core region begins to be significant.

The independent test of energy estimates can be done by the detected zenith angle distributions which have to be isotropic for different energy thresholds. In Fig. 8 the corresponding detected distributions (symbols) are compared with statistically equivalent simulated isotropic distributions (lines). The agreement of detected and simulated distributions at $E > 3 \cdot 10^6$ GeV gives an additional support to the consistency of energy estimates in the whole measurement range. The anisotropic spectral behavior at low energies ($E \sim (1-3) \cdot 10^6$ GeV) is explained by the lack of heavy nuclei at larger zenith angles in the detected flux due to the applied shower selection criteria.

Using the aforementioned unbiased ($< 5\%$) event-by-event method of primary energy evaluation (10), we obtained the all-particle energy spectrum. Results are presented in Fig. 9 (filled circle symbols, GAMMA07) in comparison with the same spectra obtained by the EAS inverse approach (line with shaded area, GAMMA06) from [6,9] and our preliminary results (point-circle symbols, GAMMA05) obtained using the 7-parametric event-by-event method with the shower core selection criteria $R < 25$m and $\theta < 30^0$ [10].

It follows from our preliminary data [10,11], that the all-particle energy spectrum derived by event-by-event analysis with the multi-parametric energy estimator (Section 3) depends only slightly on the interaction model (QGSJET01 [25] or SIBYLL2.1 [14]) and thereby, the errors of obtained spectra are mainly determined by the sum of statistical and systematic errors (7) presented in Fig. 9 by the dark shaded area.

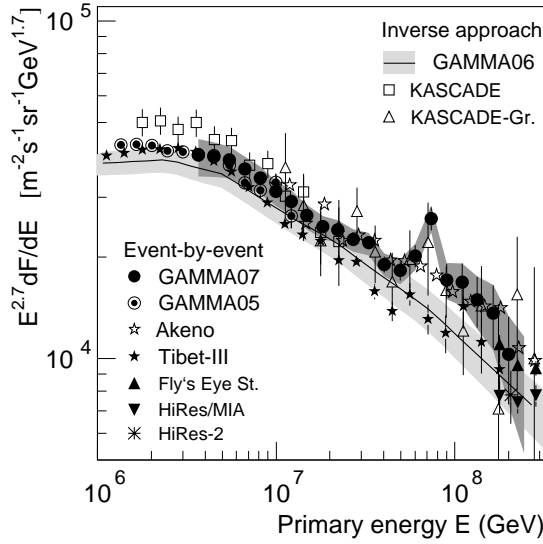Shower size detection threshold effects distort the all-particle spectrum in

13

Fig. 9. All-particle energy spectrum in comparison with the results of EAS inverse approach [6,9] and our preliminary data [10]. The AKENO, Tibet-III, Fly's Eye Stereo, Hires/MIA and Hires-2 data were taken from [2,27,28,29,30] respectively.

the range of $E < (2 - 2.5) \cdot 10^6$ GeV depending on the interaction model and determine the lower limit $E_{\min} = 3 \cdot 10^6$ GeV of the energy spectrum in Fig. 9 whereas the upper limit of the spectrum $E_{\max} \simeq (2 - 3) \cdot 10^8$ GeV is determined by the saturation of our shower detectors which begins to be significant at $E_p > 2 \cdot 10^8$ GeV and $E_{Fe} > 4 \cdot 10^8$ GeV (see Fig. 4) for primary proton and Fe nuclei. The range of minimal systematic errors and biases is $(1 - 10) \cdot 10^7$ GeV, where about 13% and 10% errors were attained (Fig. 3,4) for primary H and Fe nuclei respectively.

In Table 3 the numerical values of the obtained all-particle energy spectrum are presented along with statistical, total upper and lower errors according to (7) and corresponding number of detected events. The energy spectra for low energy region (the first four lines) were taken from our data [10] for the EAS selection criteria $R < 25$m and $\theta < 30^0$.

The obtained energy spectrum agrees within errors with the KASCADE [6], AKENO [2] and Tibet-III [27] data both in the slope and in the absolute intensity practically in the whole measurement range. Looking at the experimental points we can unambiguously point out at the existence of an irregularity in the spectrum at the energy of $(6 - 8) \cdot 10^7$ GeV. As it is seen from Figs 3 and 4, the energy estimator (10) has minimal biases ($\sim 4 - 5\%$) and errors ($\sim 0.09 - 0.12$) at this energy. With these errors the obtained bump has an apparently real nature. If we fit all our other points in the $(5 - 200) \cdot 10^6$ GeV energy range by a smooth power-law spectrum, the bin at $7.4 \cdot 10^7$ GeV exceeds this smooth spectrum by 4.0 standard deviations. The exact value for

Table 3

All-particle energy spectrum $(d\Im/dE)$ in units of $(m^2 \cdot sec \cdot sr \cdot GeV)^{-1}$ and corresponding statistical (Δ_{stat}), total upper, (Δ_+) and total lower (Δ_-) errors and number of events (N_{ev}). The first four lines represent our data [10] obtained for selection criteria $R < 25$m and $\theta < 30^0$.

$E(PeV)$	$d\Im/dE$	Δ_{stat}	Δ_+	Δ_-	N_{ev}
1.35 [10]	$0.1205E-11$	$0.11E-13$	-	-	11550
1.65 [10]	$0.7037E-12$	$0.77E-14$	-	-	8374
2.01 [10]	$0.4090E-12$	$0.54E-14$	-	-	5769
2.46 [10]	$0.2285E-12$	$0.36E-14$	-	-	3924
3.00	$0.1297E-12$	$0.52E-15$	$0.16E-13$	$0.20E-13$	59930
3.67	$0.7677E-13$	$0.37E-15$	$0.86E-14$	$0.108E-13$	43157
4.48	$0.4401E-13$	$0.25E-15$	$0.45E-14$	$0.57E-14$	30153
5.47	$0.2524E-13$	$0.17E-15$	$0.24E-14$	$0.30E-14$	20993
6.69	$0.1372E-13$	$0.12E-15$	$0.12E-14$	$0.15E-14$	13917
8.17	$0.7506E-14$	$0.77E-16$	$0.62E-15$	$0.76E-15$	9290
9.97	$0.3984E-14$	$0.51E-16$	$0.31E-15$	$0.37E-15$	5998
12.18	$0.2166E-14$	$0.34E-16$	$0.17E-15$	$0.21E-15$	3986
14.88	$0.1148E-14$	$0.23E-16$	$0.87E-16$	$0.104E-15$	2573
18.17	$0.619E-15$	$0.15E-16$	$0.45E-16$	$0.53E-16$	1692
22.20	$0.350E-15$	$0.10E-16$	$0.25E-16$	$0.29E-16$	1170
27.11	$0.1927E-15$	$0.69E-17$	$0.13E-16$	$0.15E-16$	781
33.12	$0.1101E-15$	$0.47E-17$	$0.78E-17$	$0.88E-17$	542
40.45	$0.556E-16$	$0.30E-17$	$0.42E-17$	$0.46E-17$	334
49.40	$0.306E-16$	$0.20E-17$	$0.26E-17$	$0.27E-17$	227
60.34	$0.199E-16$	$0.15E-17$	$0.18E-17$	$0.19E-17$	178
73.70	$0.149E-16$	$0.12E-17$	$0.13E-17$	$0.14E-17$	164
90.02	$0.572E-17$	$0.65E-18$	$0.70E-18$	$0.71E-18$	77
110.0	$0.326E-17$	$0.44E-18$	$0.47E-18$	$0.47E-18$	54
134.3	$0.184E-17$	$0.30E-18$	$0.31E-18$	$0.31E-18$	34
164.0	$0.94E-18$	$0.19E-18$	$0.20E-18$	$0.20E-18$	22
200.3	$0.40E-18$	$0.11E-18$	$0.12E-18$	$0.12E-18$	12
244.7	$0.243E-18$	$0.81E-19$	$0.82E-19$	$0.82E-19$	7

this significance of the bump depends somewhat on the energy range chosen to adjust the reference straight line in Fig. 9, but it lies in the range $(3.5-4.5)\sigma$.

We conservatively included the systematic errors in this estimate, although they are not independent in the nearby points but correlated: the possible overestimation of the energy in one point cannot be followed by an underestimation in the neighboring point if their energies are relatively close to each other. Systematic errors can change slightly the general slope of the spectrum but cannot imitate the fine structure and the existence of the bump.

The results from Fig. 7 show that in the range of "bump" energy ($7.4 \cdot 10^7$ GeV) the systematic errors can not increase significantly the flux. To test this hypothesis more precisely we tested the reconstruction procedure for singular energy spectra with power indices $\gamma_p = 1.5$ and $\gamma_p = 4.5$ below and above the knee energy $7.4 \cdot 10^7$ GeV in the $5 \cdot 10^7 - 10^8$ GeV energy range. Results are presented in Fig. 7 (star symbols) and show that there are no significant discrepancies of reconstructed spectra observed, which stems from high accuracy of energy reconstruction.

The detected shower sample in the bump energy region did not reveal any discrepancies with the showers from adjacent energy bins within statistical errors neither with respect to reconstructed shower core coordinates, zenith angular and χ^2 distributions, nor with respect to $\xi = N_{ch}/N_\mu$ distribution. The only difference is that the average age of showers is increased from $\bar{s} = 0.88 \pm 0.007$ at $E_0 \simeq 5 \cdot 10^7$ GeV up to $\bar{s} = 0.93 \pm 0.01$ at $E_0 \simeq 10^8$ GeV, instead of the monotonic shower age decrease with energy increment, which is observed at a low energy region ($E_0 = 3 \cdot 10^6 - 5 \cdot 10^7$ GeV).

It is necessary to note that some indications of the observed bump are also seen in KASCADE-Grande [6] (Fig. 9), TUNKA [4] and Tibet-III [27] data but with larger statistical uncertainties at the level of 1.5-2 standard deviations. Moreover, the locations of the bump in different experiments agree well with each other and with an expected knee energy for Fe-like primary nuclei according to the rigidity-dependent knee hypothesis [8,9]. However, the observed width ($\sim 20\%$ in energy) and height of the bump at the energy of $(6-8) \cdot 10^7$ GeV, which exceeds by a factor of ~ 1.5 (~ 4 standard deviations) the best fit straight line fitting all points above $5 \cdot 10^6$ GeV in Fig. 9, are difficult to describe in the framework of the conventional model of cosmic ray origin [21].

As it will be shown below (Section 5, Fig. 10,11) the detected EAS charged particle (N_{ch}) and muon size (N_μ) spectra [8,9] independently indicate the existence of this bump just for the obtained energies and as it follows from the behavior of shower age parameter versus shower size [8,9], the bump at energy $\sim 7.4 \cdot 10^7$ GeV is likely formed completely from Fe nuclei.
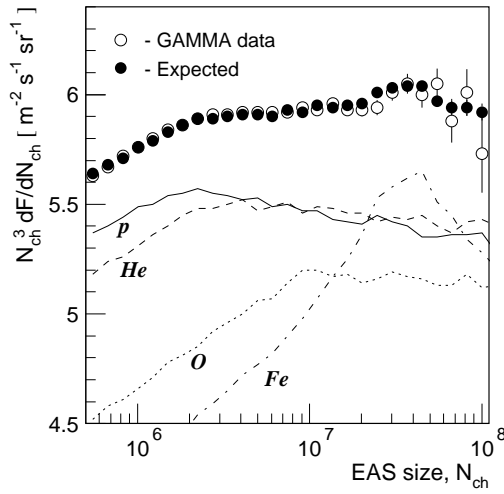
Fig. 10. EAS size spectra detected by the GAMMA facility (empty symbols) and corresponding expected spectra (filled symbols) computed in the framework of the SIBYLL2.1 interaction model and 2-component parametrization of primary spectra (11). The lines correspond to expected size spectra computed for each of primary nuclei.

5 Possible origin of irregularities

Irregularities of all-particle energy spectrum in the knee region are observed practically in all measurements [2,6,8] and are explained by both the rigidity-dependent knee hypothesis and contribution of pulsars in the Galactic cosmic ray flux [20,31,32]. Two these approaches approximately describe the all-particle spectrum in $(1 - 100) \cdot 10^6$ GeV energy region. However, the observed bump in Fig. 9 at energies $\sim 7.4 \cdot 10^7$ GeV both directly points out the presence of additional component in the primary nuclei flux and displays a very flat ($\gamma_p \sim 0 - 2$) energy spectrum before a cut-off energy $E_c \simeq 8 \cdot 10^7$ GeV.

It is known [8,9] that rigidity-dependent primary energy spectra can not describe quantitatively the phenomenon of ageing of EAS at energies $(5-10) \cdot 10^7$ GeV that was observed in the most mountain-altitude experiments [8,15,33]. It is reasonable to assume that an additional flux of heavy nuclei (Fe-like) is responsible for the bump at these energies. Besides, the sharpness of the bump (Fig. 9) points out at the local origin of this flux from compact objects (pulsars) [31,32].

The test of this hypothesis we carried out using parameterized inverse approach [7,8,9] on the basis of GAMMA facility EAS database and hypothesis of two-component origin of cosmic ray flux:
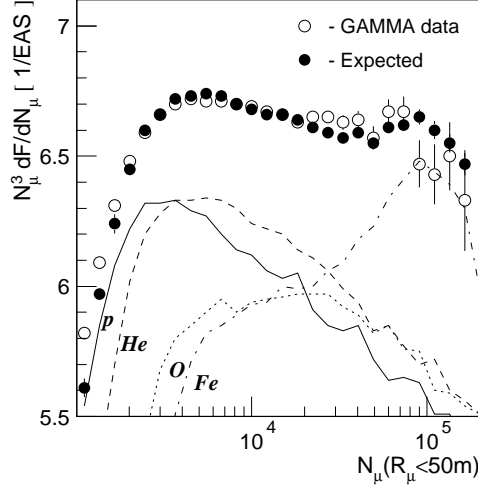
Fig. 11. The same as Fig. 10 for truncated EAS muon size spectra.

$$F_A(E) = \Phi_G(A)\Big(E_k^{-\gamma_1}\Big(\frac{E}{E_k}\Big)^{-\gamma} + P_A(E)\Big) \tag{11}$$

where $P_H = P_{He} = P_O = 0$ and

$$P_{Fe}(E) = \Phi_P(Fe) \cdot E_{c,Fe}^{-\gamma_{1p}}\Big(\frac{E}{E_{c,Fe}}\Big)^{-\gamma_p}.$$

The first term in the right hand side of expression (11) (so called Galactic component) is the power law energy spectra with rigidity-dependent knees at energies $E_k = E_R \cdot Z$ and power indices $\gamma = \gamma_1$ and $\gamma = \gamma_2$ for $E \leq E_k$ and $E > E_k$ respectively, and the second term (so called "pulsar component") is an additional power law energy spectrum with cut-off energies $E_{c,Fe}$ and power indices $\gamma_p = \gamma_{1,p}$ and $\gamma_p = \gamma_{2p}$ for $E \leq E_{c,Fe}$ and $E > E_{c,Fe}$ respectively.

The scale factors $\Phi_G(A)$ and $\Phi_P(A)$ along with particle rigidity E_R, cut-off energy $E_c(A)$ and power indices $\gamma_1, \gamma_2, \gamma_{1p}, \gamma_{2p}$ were estimated using combined approximation method [7,8,9] for two examined shower spectra showed in Figs. 10,11 (empty symbols): EAS size spectra, dF/dN_{ch} (Fig. 10) and EAS muon truncated size spectra, dF/dN_μ (Fig. 11) detected by the GAMMA facility using shower core selection criteria $\theta < 30^0$ and $r < 50$m [8,9]. We did not consider the H, He and O pulsar components to avoid a large number of unknown parameters and corresponding mutually compensative pseudo solutions [34] for the Galactic components.

The folded (expected) shower spectra (filled symbols in Figs 10,11) were computed on the basis of parametrization (11) and CORSIKA EAS simulated data set [9,8] for the $A \equiv H, He, O$ and Fe primary nuclei to evaluate the

18

Table 4

Parameters of the primary energy spectra (11) derived from combined approxima-tions of detected shower spectra. The scale factors $\Phi_{G,P}(A)$ have units of $(\text{m}^2 \cdot \text{s} \cdot \text{sr} \cdot \text{TeV})^{-1}$. The particle rigidity E_R and cut-off energies E_c are shown in PV and PeV units respectively.

Param.	G-component	P-component
$\Phi(H)$	$.102 \pm .003$	$-$
$\Phi(He)$	$.094 \pm .022$	$-$
$\Phi(O)$	$.032 \pm .015$	$-$
$\Phi(Fe)$	$.021 \pm .006$	$(.29 \pm .08) \cdot 10^{-7}$
γ_1	$2.68 \pm .005$	$1.05 \pm .5$
γ_2	$3.29 \pm .045$	$4.5 \pm .4$
E_R	$2.59 \pm .15$	$-$
$E_{c,Fe}$	$-$	76.9 ± 1.5

kernel functions of corresponding integral equations [8,9]. The computation method, was completely the same as was performed in the combined approx-imation analysis [8,9]. The initial values of spectral parameters for Galactic component were taken from [9,8] as well. In Figs. 10,11 we also presented the derived expected elemental shower spectra (lines) for primary H, He, O and Fe nuclei respectively.

The parameters of two-component primary energy spectra (11) derived from the χ^2 goodness-of-fit test of shower spectra dF/dN_{ch} and dF/dN_μ are presented in Table 4.

Resulting expected energy spectra $F_A(E)$ for the Galactic H, He, O and Fe nuclei (thin lines) along with the all-particle spectrum $\sum_A F_A(E)$ (bold line with shaded area) are presented in Fig. 12. The thick dash-dotted line corresponds to derived energy spectra of the additional Fe component (the second term in the right hand side of expression (11)). The all-particle energy spectrum obtained on the basis of the GAMMA EAS data and event-by-event multi-parametric energy evaluation method (Section 4, Fig.9) are shown in Fig.12 (symbols) as well.

It is seen, that the shape of 2-component all-particle spectrum (bold line with shaded area) calculated with parameters taken from the fit of EAS size spectra agrees within the errors with the results of event-by-event analysis (symbols) that points out at the consistency of applied spectral parametriza-tion (11) with GAMMA data.

Notice that the flux of derived additional Fe component turned out to be about $0.5 - 0.6\%$ of the total Fe flux for primary energies $E > 10^6$ GeV. This result agrees with expected flux of polar cap component [20].

The dependence of average nuclear mass number are presented in Fig. 13
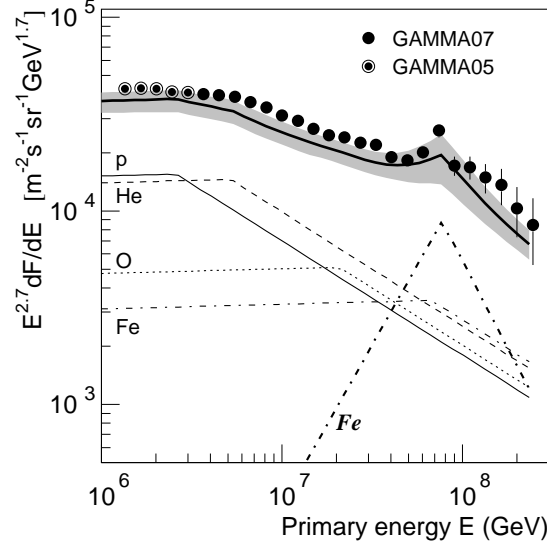
Fig. 12. All-particle primary energy spectrum (symbols) and expected energy spectra (lines and shaded area) derived from EAS inverse problem solution for p, He, O and Fe primary nuclei using 2-component parametrization (11). The thin lines are the energy spectra of Galactic H, He, O and Fe components. The thick dash-dotted line is an additional Fe component from compact objects.
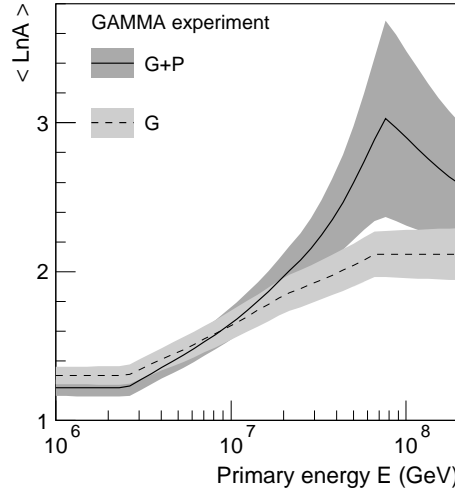

Fig. 13. Average logarithm primary nuclei mass number derived from rigidity-dependent primary energy spectra [8,9] (dashed line) and 2-component model prediction (11) taking into account additional pulsar component (solid line).

for two primary nuclei flux composition models: one-component model, where the power law energy spectra of primary nuclei have rigidity-dependent knees at particle rigidity $E_R \sim 2500$ GeV/Z [8,9] (so called Galactic component, dashed line) and two-component model (solid line), where additional pulsar (P) component was included according to parametrization (11) and data from Table 4 with very flat power index ($\gamma_{1p} \sim 1$) before cut-off energy $E_{c,Fe}$. The shaded area in Fig. 13 show the ranges of total (systematic and statistical) errors.

6 Conclusion

The multi-parametric event-by-event method (Sections 3,4) provides the high accuracy for the energy evaluation of primary cosmic ray nuclei $\sigma(E) \simeq 10-15\%$ regardless of the nuclei mass (biases$< 5\%$) in the $3-200$ PeV energy region. Using this method the all-particle energy spectrum in the knee region and above has been obtained (Fig. 9, Table 3) using the EAS database from the GAMMA facility. The results are obtained for the SIBYLL2.1 interaction model.

The all-particle energy spectrum in the range of statistical and systematic errors agrees with the same spectra obtained using the EAS inverse approach [7,6,8] in the $3-200$ PeV energy range.

The high accuracy of energy evaluations and small statistical errors point out at the existence of an irregularity ('bump') in the $60-80$ PeV primary energy region.

The bump can be described by 2-component model (parametrization (11)), of primary cosmic ray origin, where additional (pulsar) Fe component are included with very flat power law energy spectrum ($\gamma_{1p} \sim 1 \pm 0.5$) before cut-off energy $E_{c,Fe}$ (Fig. 13, Table 4). At the same time, the EAS inverse problem solutions for energy spectra of pulsar component forces the solutions for the slopes of Galactic component above the knee to be steeper (Table 4), that creates a problem of underestimation of all-particle energy spectrum in the range of HiRes [29] and Fly's Eye [28] data at $E > 200$ PeV. From this viewpoint the underestimation ($10-15\%$) of the all-particle energy spectrum (bold solid line in Fig. 12) in the range of $E > 200$ PeV can be compensated by the expected extragalactic component [35].

Though we cannot reject the stochastic nature of the bump completely, our examination of the systematic uncertainties of the applied method lets us believe that they cannot be responsible for the observed feature. The indications from other experiments mentioned in this paper provide the argument for the further study of this interesting energy region.

Acknowledgments

References

[1] Erlykin A.D., Wolfendale A.W., J. Phys. G: Nucl. Part. Phys., **23** (1997) 979; Astron. and Astrophys. **350** (1999) L1; J. Phys. G: Nucl. Part. Phys. **27** (2001) 1005.

[2] N. Nagano, T. Hara et al., J. Phys. G: Nucl. Part. Phys. **10** (1984) 1295.

[3] A.P. Garyaka, R.M. Martirosov, J. Procureur et al., J.Phys. G: Nucl. Phys. **28** (2002) 2317.

[4] E.E. Korosteleva et al., Nucl. Phys. B (Proc.Suppl.) **165** (2007) 74.

[5] T. Antoni et al., Astropart. Phys. **24** (2005) 1, (astro-ph/0505413).

[6] M. Bruggemann et al., Proc. 20th ECRS, Lisbon (2006), available from http://www.lip.pt/events/2006/ecrs/proc/ercs06-s3–77.pdf.

[7] S.V. Ter-Antonyan et al., 29th ICRC, Pune, HE1.2 **6** (2005) 101, (astro-ph/0506588).

[8] Y.A. Gallant, A.P. Garyaka, L.W. Jones et al., Proc. 20th ECRS, Lisbon (2006); available from http://www.lip.pt/events/2006/ecrs/proc/ecrs06-s4-21.pdf.

[9] A.P. Garyaka, R.M. Martirosov, S.V. Ter-Antonyan et al., Astropart.Phys. 28/2 (2007) 169 (arXiv:0704.3200v1 [astro-ph]).

[10] S.V. Ter-Antonyan et al., 29th ICRC, Pune, HE1.2, **6** (2005) 105.

[11] Y.A. Gallant, A.P. Garyaka, L.W. Jones et al., Proc. 20th ECRS, Lisbon (2006); available from http://www.lip.pt/events/2006/ecrs/proc/ecrs06-s3-95.pdf.

[12] A. Chilingarian, S. Ter-Antonian, A. Vardanyan, Nuclear Physics B, 52B, (1997) 240.

[13] V. Eganov et al., Int. Journ. of Modern Phys. A, **20**/29, (2005) 6811.

[14] R.S. Fletcher, T.K. Gaisser, P. Lipari, T. Stanev, Phys.Rev. **D50** (1994) 5710.

[15] V.V. Avakian et al., Proc. 24th Intern. Cosmic Ray Conf., Rome, **1** (1995) 348.

[16] V.S. Murzin, L.I. Sarycheva, Cosmic rays and their interactions, (1968), Atomizd, Moscow (in Russian).

[17] M. Aglietta et al., EAS-TOP Collaboration, Astropart. Phys. 10 (1999) 1.

[18] M.A.K. Glasmacher et al., Astropart. Phys. 10 (1999) 291.

[19] M. Amenomori et al., 29th ICRC, Pune, HE12(2005) (29icrc/PAPERS/HE12/jap-katayose-Y-abs2-he12-poster.pdf).

[20] T. Stanev, P.L. Biermann, T.K. Gaisser, Astron. Astrophys. 274 (1993) 902.

[21] A.M. Hillas, J. Phys. G: Nucl. Part. Phys. 31 (2005) R95.

[22] B. Peters, Nuovo Cimento 14 (Suppl.) (1959) 436.

[23] J.R. Hörandel, Astropart. Phys. 21 (2004) 241.

[24] D. Heck, J. Knapp, J.N. Capdevielle, G. Schatz, T. Thouw, Forschungszentrum Karlsruhe Report, FZKA 6019 (1998).

[25] N.N. Kalmykov, S.S. Ostapchenko, Yad. Fiz. **56** (1993) 105 (in Russian).

[26] A. Fasso, A. Ferrari, S. Roesler et al., hep-ph/0306267 (http://www.fluka.org).

[27] M. Amenomori, X.J. Bi, D. Chen et al., arXiv:0801.1803 [hep-ex] (2008).

[28] D.J. Bird et al., Astrophys. J. 441 (1995) 144.

[29] T. Abu-Zayyad et al., Astrophys. J. 557 (2001) 557.

[30] R.U. Abbassi et al., astro-ph/0208301 (2002).

[31] A.D. Erlykin and A.W. Wolfendale, Astropart. Phys., 22/1 (2004) 47 (astro-ph/0404530).

[32] W. Bednarek, R.J. Protheroe, Astropart.Phys. **16** (2002) 397.

[33] S. Miyake, N. Ito et al., Proc. 16th ICRC, Kyoto, **13** (1979) 171.

[34] S.V. Ter-Antonyan, Astropart. Phys. **28**, 3 (2007) 321.

[35] T.K. Gaisser, arXiv: astro-ph/0501195 (2005).